

# Heavy-Fermion Behavior and a Tunable Density Wave in a Novel Vanadium-based Mosaic Lattice

Yusen Xiao<sup>1\*</sup>, Zhibin Qiu<sup>3,4\*</sup>, Qingchen Duan<sup>1</sup>, Zhaoyi Li<sup>3,4</sup>, Hengxin Tan<sup>2</sup>, Shu Guo<sup>3,4†</sup>, and Ruidan Zhong<sup>1,2†</sup>

<sup>1</sup> *Tsung-Dao Lee Institute, Shanghai Jiao Tong University, Shanghai 201210, People's Republic of China.*

<sup>2</sup> *School of Physics and Astronomy, Shanghai Jiao Tong University, Shanghai 200240, People's Republic of China.*

<sup>3</sup> *Shenzhen Institute for Quantum Science and Engineering, Southern University of Science and Technology, Shenzhen 518055, China.*

<sup>4</sup> *International Quantum Academy, Shenzhen 518048, China.*

*\*These authors contribute equally to this work.*

*†E-mail: rzhong@sjtu.edu.cn; guos@sustech.edu.cn*

The pursuit of geometrically frustrated lattices beyond conventional paradigms remains a central challenge in the design of quantum materials. Herein, we report the discovery of  $\text{Cs}_3\text{V}_9\text{Te}_{13}$  (CVT), a novel intermetallic compound that hosts a unique two-dimensional vanadium “mosaic lattice”, composed of an ordered tessellation of triangles, squares, and pentagons, bearing profound structural kinship with the celebrated kagome lattice. Remarkably, CVT exhibits behavior analogous to heavy fermion systems, characterized by a large Sommerfeld coefficient ( $\gamma \approx 425 \text{ mJ mol}^{-1}\text{K}^{-2}$ ) and a coherent density-wave-like (DW-like) transition at  $T^* = 47 \text{ K}$ . This establishes CVT as a rare and intriguing example of a strongly correlated system. Inspired by pressure-tuning in related compounds, we demonstrate that this ground state is exquisitely tunable via chemical pressure. Systematic substitution of Cs with smaller Rb ions suppresses the DW-like order while strongly weakening the heavy-electron response, ultimately driving the system into a distinct non-magnetic, semiconducting, quantum-disordered state above 60 mK. This work unveils a new arena for exploring the interplay between heavy-fermion physics, density waves, and quantum disorder. The mosaic lattice in  $\text{Cs}_3\text{V}_9\text{Te}_{13}$  provides an unprecedented, chemically controllable platform for navigating the phase space between distinct correlated electronic states.

## Introduction

The interplay between lattice geometry and electronic correlations is a cornerstone of modern condensed matter physics. Archimedean lattices<sup>1,2</sup>, such as triangular, square, and honeycomb networks, have long served as fundamental playgrounds for emerging phenomena ranging from high- $T_c$  superconductivity<sup>3,4</sup> to Dirac fermions<sup>5,6</sup>. Among these, the kagome lattice has recently ascended to prominence. Its geometry of corner-sharing triangles naturally combines geometric frustration<sup>7</sup>, non-trivial band topology<sup>8,9</sup>, and flat electronic bands<sup>10</sup>, providing fertile ground for exotic quantum states. Recent discoveries of  $AV_3Sb_5$  ( $A = K, Rb, Cs$ ) family have substantiated this potential, revealing unconventional charge density wave (CDW), potential time-reversal symmetry breaking (TRSB), pair density wave (PDW), and superconductivity<sup>8,11–14</sup>. In the related magnetic compound  $CsCr_3Sb_5$ , pressure suppresses density-wave order and induces superconductivity, accompanied by quantum critical behavior and enhanced quasiparticle mass renormalization<sup>15</sup>, underscoring the intimate coupling between lattice geometry and electronic correlation.

Despite these advances, however, the structural landscape of two-dimensional periodic lattices extends far beyond conventional Archimedean tiling. Regular pentagons cannot tile the plane without distortion<sup>16,17</sup>, imposing fundamental geometric constraints on periodic crystalline frameworks. As a result, ordered integration of pentagonal motifs into extended two-dimensional lattices remains exceptionally rare, and their influence on correlated electronic states is largely unexplored.

Here we report  $Cs_3V_9Te_{13}$  (CVT), a vanadium-based intermetallic compound that realizes a previously unreported two-dimensional “mosaic lattice”—an ordered tessellation of triangles, squares, and pentagons. This architecture introduces a pentagon-integrated periodic framework that is structurally related to, yet distinct from, the kagome network, thereby expanding the geometric design space of frustrated lattices. CVT exhibits pronounced electronic correlations, including a coherent density-wave-like transition at  $T^* = 47$  K and an exceptionally large Sommerfeld coefficient  $\gamma = 425$  mJ mol<sup>-1</sup> K<sup>-2</sup>. The magnitude of  $\gamma$  indicates substantial quasiparticle mass renormalization in a purely  $d$ -electron system, placing CVT among the rare  $d$ -electron materials exhibiting heavy-fermion-like behavior. The correlated ground state is tunable via chemical pressure: systematic substitution of Cs with smaller Rb ions suppresses the density-wave-like transition and reduces the heavy-electron response. Upon full suppression of the ordered state, the system evolves into a non-magnetic, semiconducting state. These results position the CVT mosaic lattice as a new structural platform for realizing and tuning heavy-electron behavior and quantum criticality in a purely  $d$ -electron environment.

## Results and Discussion

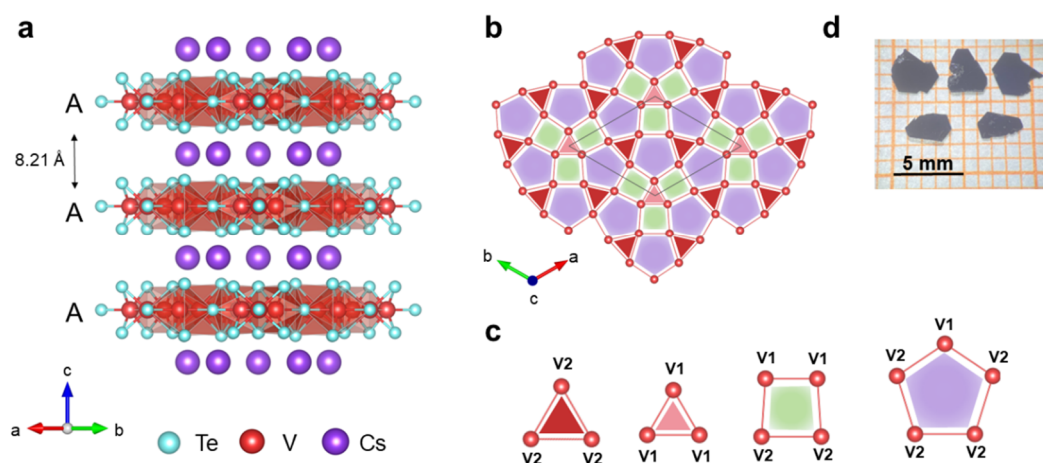


**Figure 1 Crystal structure.** (a) 3D framework of CVT. (b) The V-based 2D mosaic Lattice (c) Constituent triangular, square, and pentagonal units in a 2D mosaic Lattice. (d) Photograph of CVT single crystals.

A millimeter-sized, air-stable, high-quality single crystal of CVT was obtained via a self-flux method (**Figure 1d**). The crystal structure, determined by single-crystal X-ray diffraction (SC-XRD), crystallizes in the hexagonal crystal system with the centrosymmetric space group of  $P-62m$  (No.189). Detailed crystallographic details are provided in **Table S1-2** and **Figure S2**. Notably, upon cooling from 300 to 30 K, only a slight lattice variation was observed, with no indication of a change in crystal symmetry, providing compelling evidence for the absence of a crystal structural transition across the entire temperature range. As a representative, the crystal structure refined at 300 K from SC-XRD was used for the following discussion. From a structural perspective, CVT adopts a V-based 2D layered architecture, with nonmagnetic Cs ions located between the layers and serving as spacers (**Figure 1a**). In the asymmetric unit of CVT, there are three unique Te sites ( $3g$ ,  $4h$ ,  $6i$ ), one unique Cs site ( $3f$ ), and two unique V sites ( $3h$ ,  $6k$ ). As shown in **Figures 1b** and **1c**, the 2D mosaic layer in CVT can be described as a network of two types of triangles, one type of square, and one type of pentagon. Each V-based triangle connects to three squares and three pentagons via either edge-sharing or corner-sharing. Five-fold rotational symmetry is crystallographically forbidden. To accommodate such a unique geometry within a 2D plane, the lattice adopts a mixed tiling of triangles, squares, and pentagons. The V-V bond distances across the five edges of the pentagon vary from 3.02 to 3.19 Å, which further distorts the pentagon away from a regular structure. Powder X-ray diffraction (P-XRD) measurement on a single crystal sample shows (00L) diffraction peaks, confirming the sample is in a single phase with its natural growth face as the  $ab$ -plane. In addition, to further verify the structure and phase purity, Rietveld refinement was performed on polycrystalline

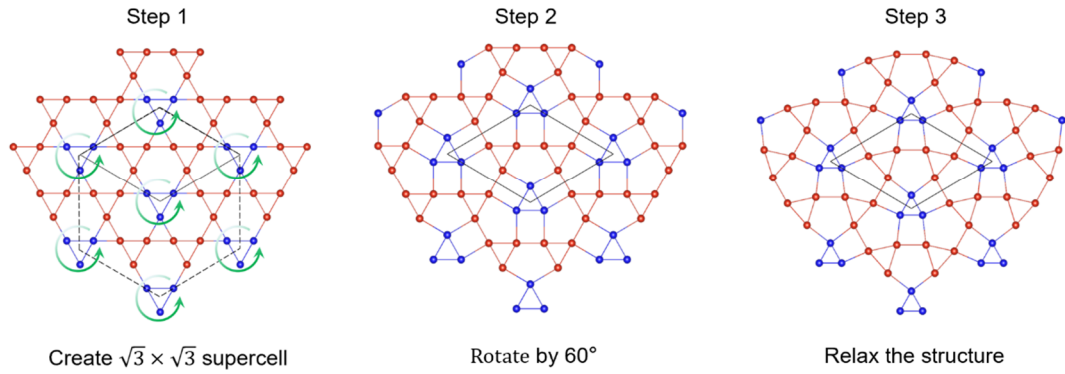


**Figure 2 Structural transformation from 2D kagome to mosaic-like lattice.** Left: prototype of the kagome lattice. Center: regular mosaic-like lattice. Right: relaxed mosaic-like lattice.

sample synthesized by solid state reaction (**Figure S1**).

The geometry of a mosaic lattice is fundamentally entwined with its electronic ground states. To elucidate the origin of this complex tiling, it is instructive to compare it with the prototypical kagome lattice in  $AV_3Sb_5$ . Our mosaic lattice could also be described from a transformation product of an ideal kagome lattice (**Figure 2**): first, atoms in the ideal kagome lattice can be divided into two groups (blue triangular and the remaining red vanadium atoms) to create a  $\sqrt{3} \times \sqrt{3}$  supercell (Step 1), and then all blue triangles are rotated by  $60^\circ$  (clockwise or counterclockwise) to generate a highly symmetric mosaic-like lattice (Step 2). After full structural relaxation, the resulting geometry reproduces the mosaic lattice observed in CVT (Step 3). Notably, this resulting mosaic lattice retains the intrinsic geometric frustration of the parent kagome network while introducing a higher degree of topological complexity. This structural metamorphosis not only expands the crystal unit cell but also fundamentally renormalizes the hopping parameters and electronic structure, providing a fertile platform for the electronic correlation effects and heavy-fermion-like behavior discussed hereafter.

The physical properties of the mosaic vanadium network were systematically investigated through comprehensive measurements (**Figure 3**). As shown in **Figure 3a**, the magnetic susceptibility ( $\chi$ ) reveals a distinct anomaly at  $T^* = 47$  K, with the high-temperature data (70-150 K) following a Curie-Weiss-like behavior (**Figure 3a inset**). The fitting yields  $\chi_0 = 0.0044$  emu/mol, a Weiss temperature of  $\theta_{ab} = -42$  K, indicating dominant antiferromagnetic interactions, and an effective magnetic moment of  $\mu_{\text{eff}} = 0.58 \mu_B/\text{V}$ . This value, while suppressed relative to localized V ions, is notably larger than in the  $AV_3Sb_5$  kagome family ( $\sim 0.2 \mu_B/\text{V}$ ), where uniform short V-V bonds ( $\sim 2.7$  Å) enable strong  $3d$  orbital overlap and large bandwidths,

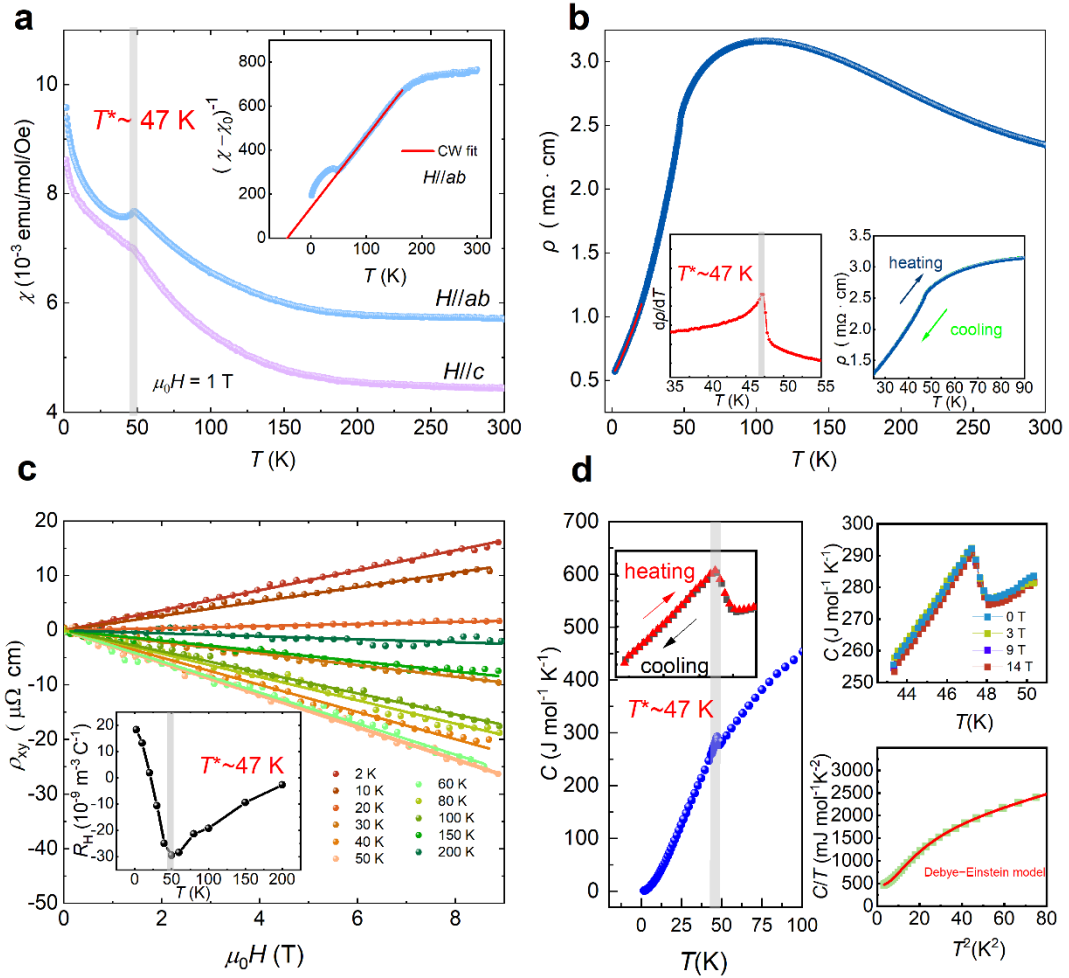


**Figure 3 Elementally Physical Properties of CVT.** (a) Temperature-dependent magnetic susceptibility measured in an applied field of  $\mu_0 H = 1$  T under zero-field-cooled (ZFC) conditions. The inset shows the Curie-Weiss fit to the inverse susceptibility data. (b) Temperature-dependent resistivity  $\rho(T)$ . Inset shows  $d\rho/dT$  (left) and  $\rho(T)$  hysteresis between cooling and warming cycles (right). (c) Hall resistivity  $\rho_{xy}$  at selected temperatures, determined via  $\rho_{xy} = [\rho_{xy}(+H) - \rho_{xy}(-H)]/2$  to eliminate the longitudinal component. Inset: Temperature dependence of the Hall coefficient  $R_H$ . (d) Temperature-dependent specific heat. Inset: specific heat measured during heating and cooling cycles. Upper right: specific heat under various applied magnetic fields. Lower right: Fit to the data in the range 1.8-8 K using the Debye-Einstein model.

resulting in a non-magnetic itinerant metallic state<sup>14,18,19</sup>. In  $\text{Cs}_3\text{V}_9\text{Te}_{13}$ , however, the vanadium network is highly anisotropic, featuring both short ( $d_{\text{V1-V1}} \approx 2.7\text{\AA}$ ) and significantly elongated ( $d_{\text{V1-V1}} \approx 3.2\text{\AA}$ ) V-V distances (**Figure S2**). To understand this magnetic behavior, we consider the mixed-valence nature indicated by XPS measurements (**Figure S3**). The V  $2p_{3/2}$  spectrum shows features at  $\sim 512.4$ ,  $515.8$ , and  $516.7$  eV, corresponding to  $\text{V}^0$ ,  $\text{V}^{3+}$ , and  $\text{V}^{4+}$  ions states, respectively, evidencing their potential coexistence<sup>20</sup>. Although only two symmetry-inequivalent V sites (V1 and V2) are identified in the room-temperature average structure, the emergence of three valence states suggests a potential charge disproportionation or symmetry

lowering associated with the CDW transition. Specifically, the V2 site likely undergoes a subtle structural modulation or splitting below  $T^*$ , providing distinct local environments for  $V^{3+}$  and  $V^{4+}$  ions. While the  $V^0$  species and the electrons within the short-bond sublattices contribute to the itinerant background, the localized  $V^{3+}$  ( $d^2$ ,  $S=1$ ) and  $V^{4+}$  ( $d^1$ ,  $S=1/2$ ) ions associated with the expanded V-V environments likely harbor local moments. The experimentally obtained effective moment is smaller than the corresponding spin-only values ( $2.83 \mu_B$  for  $V^{3+}$ ,  $1.73 \mu_B$  for  $V^{4+}$ ), which is a common feature in metallic systems where Hund's rule coupling or valence fluctuations partially suppress the local moments<sup>21</sup>. The relatively enhanced  $\mu_{\text{eff}}$  compared with the kagome metal  $AV_3Sb_5$  highlights the significant role of site-selective localization and electronic correlations within this mosaic lattice.

The temperature dependent electrical resistivity  $\rho(T)$  of CVT exhibits non-monotonic behavior characteristic of bad-metal transport (**Figure 3b**), similar to that observed in  $CsCr_3Sb_5$ <sup>15,22</sup>. At high temperatures ( $T \gtrsim 100$  K),  $\rho(T)$  displays weak temperature dependence with values reaching  $\sim 3.1$  m $\Omega$  cm, indicative of incoherent electron scattering. Upon cooling, a pronounced kink emerges at  $T^* = 47$  K, followed by a sharp metallic decrease at lower temperatures. The resistive anomaly exhibits negligible thermal hysteresis and remains insensitive to magnetic fields up to 5 T (**Figure 3b inset**, **Figure S4**). Low-temperature transport ( $T < 30$  K) is quantified by fitting  $\rho = \rho_0 + AT^n$ , yielding  $\rho_0 = 0.54$  m $\Omega$  cm,  $A = 0.014$  m $\Omega$  cm, and  $n \approx 1.2$ , significantly deviating from the Fermi-liquid expectation ( $n = 2$ ) and pointing to strong electronic correlations. Notably, the Hall coefficient  $R_H$  shows a sharp drop at  $T^* \approx 47$  K, signaling substantial Fermi surface reconstruction and possible changes in carrier density or mobility. Upon further cooling,  $R_H$  reverses sign, establishing hole-dominated conduction in the low-temperature regime (**Figure 3c**). Additionally, magnetoresistance at 2 K exhibits a small negative MR of  $\sim -1.2\%$  at 9 T (**Figure S5**), suggesting minor contributions from spin-dependent scattering in the strongly correlated regime.

Specific heat measurements provide direct thermodynamic insight into the nature of the phase transition (**Figure 3d**). A pronounced  $\lambda$ -type anomaly is observed at  $T^* = 47$  K, without detectable thermal hysteresis, indicating a second-order or weakly first-order phase transition. This is consistent with the absence of any detectable structural phase transition in low-temperature single-crystal X-ray diffraction (SXRD) measurements down to 30 K. The transition temperature remains essentially unchanged under magnetic fields up to 14 T, indicating that the transition is not driven by conventional local-moment magnetism. After subtracting the phonon background, the entropy change associated with the transition, obtained from  $\Delta S = \int \Delta C/T dT$ , reaches  $\Delta S \approx 1.0$  J mol<sup>-1</sup> K<sup>-1</sup> (**Figure S6**). The relatively small entropy

change suggests that the transition involves a limited subset of electronic states. The low-temperature  $C/T$  versus  $T^2$  data show clear deviation from linearity. We therefore employ a combined Debye-Einstein model<sup>23</sup> to describe the specific heat, fitting the data to

$$\frac{c_p(T)}{T} = \gamma + \beta T^2 + 3R\delta \frac{(\Theta_E/T)^2 e^{\Theta_E/T}}{T[e^{\Theta_E/T} - 1]^2},$$

in which the first two terms originate from the standard Debye model, while the third term represents the contribution of an Einstein mode. The fit yields parameters  $\gamma = 425 \text{ mJ mol}^{-1} \text{ K}^{-2}$ ,  $\beta = 14.1 \text{ mJ mol}^{-1} \text{ K}^{-4}$ , and  $\Theta_E = 22.8 \text{ K}$ . The Sommerfeld coefficient  $\gamma$  substantially exceeds values for the prototypical kagome metal  $\text{CsV}_3\text{Sb}_5$  ( $\gamma \sim 20 \text{ mJ mol}^{-1} \text{ K}^{-2}$ )<sup>24</sup> and the strongly correlated system  $\text{CsCr}_3\text{Sb}_5$  ( $\gamma \sim 105 \text{ mJ mol}^{-1} \text{ K}^{-2}$ )<sup>15</sup>, and is comparable in magnitude to that reported for  $\text{LiV}_2\text{O}_4$  ( $\gamma \sim 420 \text{ mJ mol}^{-1} \text{ K}^{-2}$ ), the rare  $d$ -electron heavy Fermion system driven by correlation-induced flat bands arising from intra-atomic Hund's coupling<sup>25,26</sup>. Such a large Sommerfeld coefficient indicates a pronounced enhancement of the electronic effective mass and strong electronic correlations within the mosaic lattice, suggesting the possible emergence of a  $d$ -electron heavy-fermion state. Collectively, the magnetic susceptibility, electrical transport, and specific heat measurements reveal a strongly correlated electronic state and indicate a DW-like bulk phase transition at  $T^*$ .

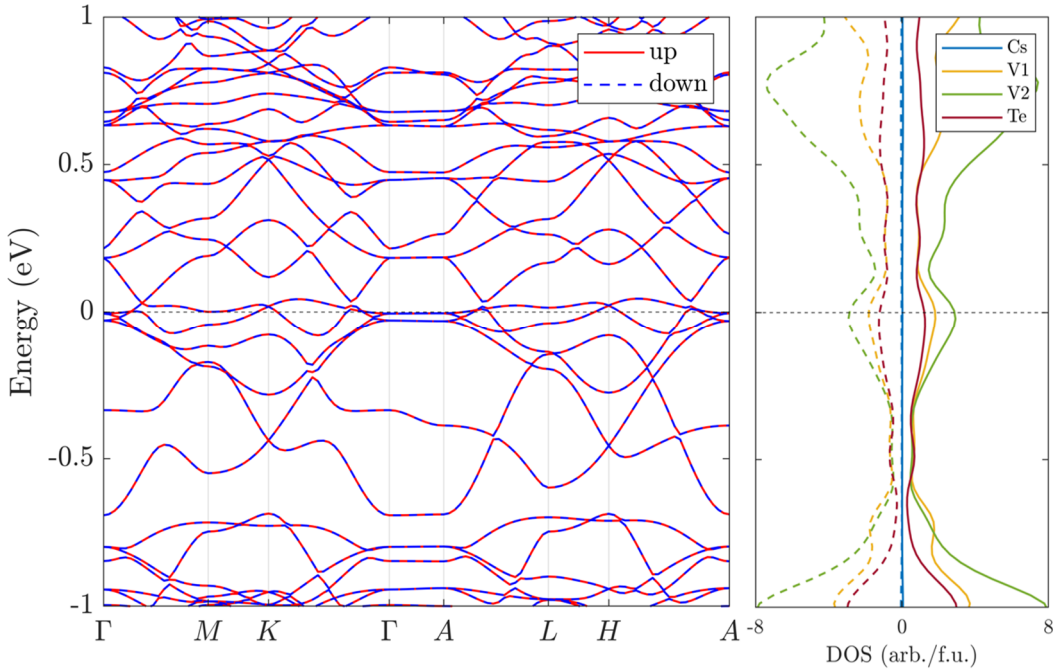


**Figure 4** First-principles electronic structure calculations of CVT. Left: band structure where up and down represent the two spin channels. Right: density of states (DOS), position values for the spin up channel and negative ones for the spin down channel. Spin-orbit coupling is not included.

Electronic structure calculations provide crucial insight into the properties of CVT (**Figure 4**). The calculated band structure and density of states (DOS) within the antiferromagnetic interaction (ferromagnetic configuration in the *ab* plane and antiferromagnetic configuration along the out-of-plane direction) framework indicate a metallic character, with multiple bands crossing the Fermi level. Near the Fermi level, the electronic states are dominated by V *3d* orbitals, and Dirac points emerge at the K points of the Brillouin zone (BZ), van Hove singularities (vHSs) are present at the M points, and flat bands are observed within the  $\Gamma$ -M-K plane. These features are analogous to those recently reported in kagome superconductors  $AV_3Sb_5$ <sup>27,28</sup> and  $CsCr_3Sb_5$ <sup>15</sup>, and the kagome metal  $ScV_6Sn_6$ <sup>29</sup>. The total DOS at the Fermi level,  $D(E_F)$ , is determined to be  $15 \text{ eV}^{-1} \text{ f.u.}^{-1}$ , significantly exceeding values typical of conventional kagome systems. From this, the band-derived Sommerfeld coefficient is calculated as  $\gamma_{\text{band}} = (\pi^2 k_B^2 / 3) D(E_F) = 35 \text{ mJ mol}^{-1} \text{ K}^{-2}$  per formula unit. Strikingly, the experimental value  $\gamma$  surpasses  $\gamma_{\text{band}}$  by approximately a factor of 12, indicating pronounced electron mass renormalization due to strong electronic correlations.

The electronic ground states of kagome-related materials often exhibit a remarkable sensitivity to lattice parameters. A prominent example is the  $CsCr_3Sb_5$  family, where the application of physical pressure effectively tunes the system from a non-superconducting state into a superconducting one<sup>15</sup>, we employed chemical pressure to modulate the mosaic lattice by substituting the  $Cs^+$  ions in CVT with smaller  $Rb^+$  ions (**Figure 5**), thereby exploring the evolution of the correlated state under structural compression. This ionic substitution leads to a dramatic contraction of the interlayer spacing, with the *c*-axis shrinking from 8.21 Å to 7.93 Å (**Figure 5a**). Concomitantly, the stacking sequence evolves from an A-A-A pattern (space group  $P-62m$ ) to a staggered A-B-A-B configuration ( $Cmcm$ ). Despite that the vanadium layers retain the same mosaic lattice, on a local scale the vanadium trimers lose their equilateral symmetry and undergo significant distortion, as evidenced by the inequivalent V-V bond lengths in the Rb-analogue (**Figure 5b**). Detailed crystallographic details are provided in **Table S3-4** and **Figure S7-8**.

The physical properties of RVT diverge sharply from those of its Cs-counterpart. In stark contrast to the metallic CVT, RVT exhibits a semi-insulating behavior with a substantial activation energy  $E_a \approx 215 \text{ meV}$  (**Figure 5c**), indicating a transition toward more localized electronic states. The magnetic susceptibility  $\chi(T)$  (**Figure 5d**) reveals no sharp phase transition down to 1.8 K, while a Curie-Weiss fit to the high-temperature (100-300 K) yields a large negative Weiss temperature  $\theta_{ab} = -248 \text{ K}$  and an effective moment  $\mu_{\text{eff}} = 0.94 \mu_B/\text{V}$ . These values

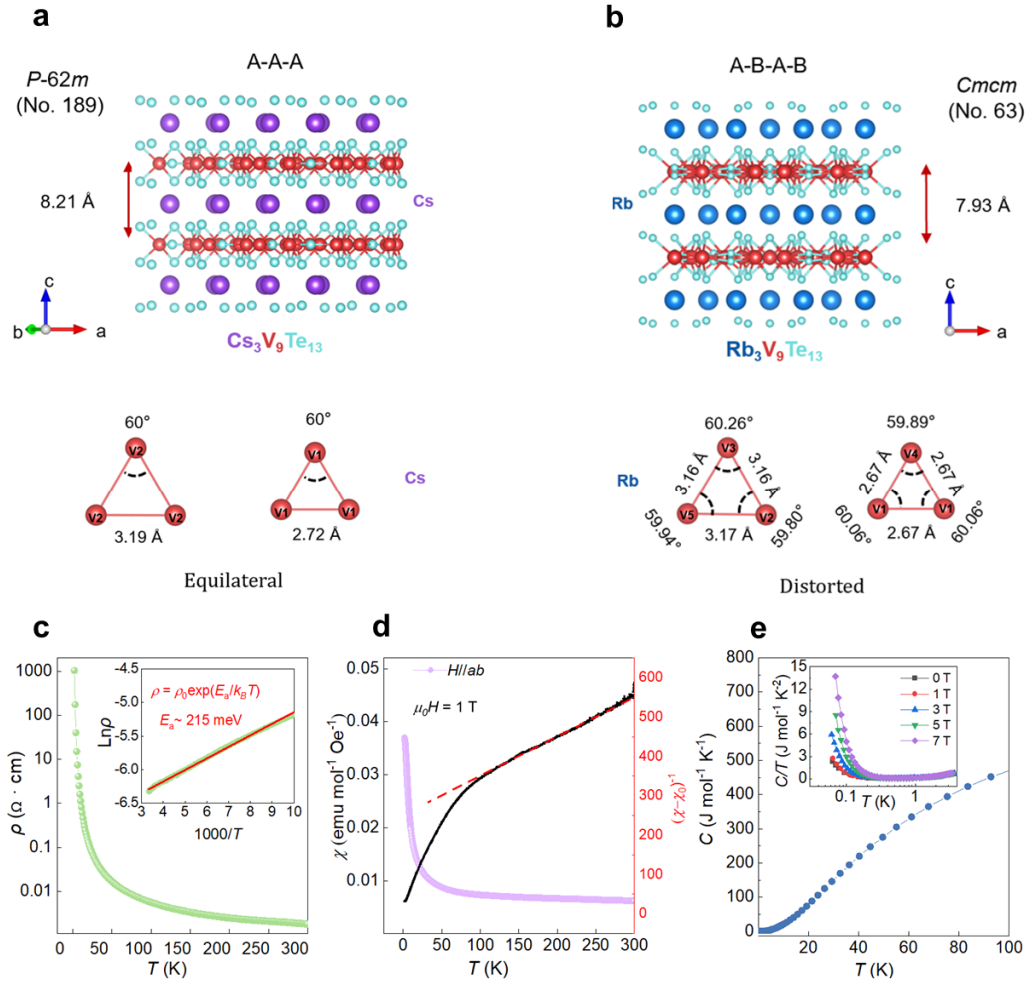


**Figure 5** Structural comparison between CVT and RVT with elementary physical properties of RVT. (a) The schematic full crystal structure of  $Cs_3V_9Te_{13}$  and  $Rb_3V_9Te_{13}$ . (b) The equilateral and distorted triangulars in CVT and RVT, respectively. (c) Temperature dependence of the electrical resistivity for RVT. The inset displays the plot of  $\ln(\rho)$  against temperature, analyzed according to the Arrhenius equation. Temperature-dependent magnetic susceptibility (ZFC) data for RVT with fields of  $\mu_0 H = 1$  T. Inset: (d) Temperature-dependent inverse susceptibility  $(\chi - \chi_0)^{-1}$ . The solid line represents a Curie-Weiss fit to the data. (e) Temperature-dependent specific heat for RVT. The inset shows specific heat under different magnetic fields ranges from 60 mK to 3.8 K.

signify dominant antiferromagnetic interactions and an inherent magnetic frustration. The absence of long-range order is further confirmed by heat capacity measurements (**Figure 5e**), which show no  $\lambda$ -like anomaly down to 60 mK. Given the large AFM exchange correlations, the resulting frustration parameter  $f = |\theta|/T_N$  exceeds  $10^3$ , placing RVT in the regime of highly frustrated magnets<sup>7</sup>. Below 1 K, the phonon contribution becomes negligible. A sharp upturn in the zero-field specific heat emerges below approximately 0.15 K that enhances with magnetic fields (**Figure 5e inset**), consistent with a nuclear Schottky contribution ( $C_{nuc} = AT^2$ ). After

subtracting this component, the remaining magnetic specific heat follows a  $C_{\text{mag}} \propto T^n$  power law with  $n \approx 2$  in the zero-temperature limit (**Figure S9**). This  $T^2$  dependence is suggestive of gapless spin excitations with linear dispersion, a behavior commonly observed in highly frustrated magnetic systems and quantum spin liquid (QSL) candidate materials<sup>30,31</sup>. Collectively, these results demonstrate that the 'chemical pressure' exerted by Rb-substitution not only collapses the interlayer spacing but also quenches the itinerant heavy-fermion state of the mosaic lattice, fostering a highly frustrated, localized quantum magnetic ground state.

## Conclusion and Outlook

In summary, we have synthesized and characterized a new family of vanadium-based compounds,  $A_3V_9Te_{13}$  ( $A = \text{Cs, Rb}$ ), which features a unique mosaic-lattice geometry, composed of an ordered tessellation of triangles, squares, and pentagons. Our investigation reveals that  $\text{Cs}_3\text{V}_9\text{Te}_{13}$  undergoes a prominent phase transition at  $T^* = 47$  K, characterized by an itinerant-to-correlated crossover and a reconstructed Fermi surface. This transition is accompanied by pronounced quasiparticle mass renormalization, as indicated by the exceptionally large Sommerfeld coefficient  $\gamma = 425$  mJ mol<sup>-1</sup>K<sup>-2</sup>, which is suggestive of heavy-fermion behavior in this purely d-electron system. The enhanced effective magnetic moment in the Cs system, compared to nearly non-magnetic kagome  $AV_3\text{Sb}_5$  compounds, highlights the robust electronic correlations inherent to the mosaic framework.

Furthermore, we demonstrate that the electronic properties of this lattice are highly tunable via chemical pressure. Substituting Cs with Rb systematically suppresses the  $T^*$  transition and quenches the heavy-quasiparticle response. Upon complete suppression of the ordered state, the system evolves into a non-magnetic, semiconducting regime characterized by strong antiferromagnetic interactions and extreme magnetic frustration. The Rb analogue exhibits no long-range magnetic order down to 60 mK, with magnetic specific heat following a  $C_{\text{mag}} \propto T^2$  power law possible suggestive of gapless spin excitations with linear dispersion. Collectively, the  $A_3V_9Te_{13}$  family provides a versatile platform for exploring the interplay between geometric frustration and strong electron correlations.

The discovery of the  $A_3V_9Te_{13}$  family opens several promising avenues for future research. A key priority among these is to clarify the microscopic nature of the  $T^* = 47$  K anomaly in  $\text{Cs}_3\text{V}_9\text{Te}_{13}$ , for which variable-temperature transmission electron microscopy (TEM) and scanning tunneling microscopy (STM) are crucial. Given the structural sensitivity of the electronic states, physical pressure or uniaxial strain experiments are highly warranted. Such

studies could potentially suppress the  $T^*$  transition to induce unconventional superconductivity, similar to the behavior observed in related vanadium- or chromium-based kagome systems<sup>15,32</sup>. Besides, the origin of the gapless excitations in  $\text{Rb}_3\text{V}_9\text{Te}_{13}$  requires further clarification. Microscopic probes such as muon spin resonance ( $\mu\text{SR}$ ) and inelastic neutron scattering (INS) will be essential for mapping the low-energy spin dynamics and determining whether the system represents a quantum spin liquid or a novel form of disordered magnetism. Finally, comprehensive theoretical studies focusing on the flat-band physics and orbital-selective correlations of the mosaic lattice are needed. Unraveling how the specific trimer-based geometry influences the competition between localized and itinerant degrees of freedom will be key to understanding the rich phase diagram of these materials.

## Methods

**Single Crystal Growth:** Single crystals of  $\text{Cs}_3\text{V}_9\text{Te}_{13}$  were grown using a flux method. Starting materials, including Cs or Rb pieces (2N), V powder (3N), and Te lumps (5N) with a total mass of 3 g, were weighed according to a molar ratio of (Cs or Rb) : V : Te = 7 : 3 : 12. The mixture was then loaded into an alumina crucible, which was subsequently sealed in a tantalum tube under an argon atmosphere. The tantalum tube was finally encapsulated in an evacuated quartz ampoule. The assembly was heated to 1000 °C over 15 hours, held at this temperature for 24 hours, and then slowly cooled to 650 °C at a rate of 2 K/h. Finally, the system was allowed to cool to room temperature naturally inside the furnace. The obtained crystals appeared as thin, black plates. The polycrystalline sample was synthesized using a procedure similar to that for the single crystal. Stoichiometric amounts of the constituent elements were mixed according to the chemical formula, slowly heated to 900 °C, and annealed for 48 h to obtain the polycrystalline powder. All sample handling procedures were performed inside an argon-filled glovebox ( $\text{H}_2\text{O}$  and  $\text{O}_2$  levels < 0.1 ppm).

**Single Crystal X-ray Diffraction (SC-XRD):** The single crystal X-ray diffraction (SC-XRD) was performed using a single crystal X-ray diffractometer (D8 VENTURE, Bruker) under both 300 K and 100 K with a  $\text{N}_2$ -based cryo cooling system. The PHOTON III C14 detector captured graphite-monochromatized Mo  $K_\alpha$  radiation with a wavelength of 0.71073 Å. At 30 K, the SC-XRD pattern was collected using a PHOTON II diffractometer with a multilayer mirror monochromatized Mo  $K_\alpha$  radiation ( $\lambda = 0.71073$  Å) and a He-based cryocooling system. APEX4 software was utilized to correct the raw data. The ShelXT structure solution program was used to solve the structures using direct methods, and the ShelXL least-squares refinement

package in the Olex2 program was employed to refine the structure<sup>33</sup>. The PLATON program's ADDSYM algorithm was applied to detect any possible higher symmetry, but no missing symmetry was found for the above materials<sup>34</sup>. The related crystallographic data are summarized in **Tables S1-S4**.

**Powder X-ray diffraction (P-XRD):** Powder XRD data were collected at room temperature on a Bruker D8 Advance Eco diffractometer using Cu-K $\alpha$  radiation ( $\lambda = 1.5418 \text{ \AA}$ ) over a 2 $\theta$  range of 10 $^\circ$  to 90 $^\circ$  (**Figures S1 and S7**).

**X-ray photoelectron spectroscopy (XPS):** XPS measurements were performed using a Thermo K-Alpha spectrometer. Samples were prepared, cleaved, and handled entirely in an argon-filled glovebox to avoid air exposure, and then transferred to the instrument under inert conditions.

**Physical Property Measurement System (PPMS):** Magnetic, transport, and thermal properties were characterized using a Quantum Design PPMS. DC magnetic susceptibility was measured on a single crystal of Cs<sub>3</sub>V<sub>9</sub>Te<sub>13</sub> and Rb<sub>3</sub>V<sub>9</sub>Te<sub>13</sub> from 1.8 to 300 K under various magnetic fields. Electrical resistivity within the *ab* plane was determined by the standard four-probe method. The Hall coefficient was determined by sweeping the magnetic field from positive to negative at a fixed temperature, with the magnetoresistance component subtracted. Specific heat capacity was measured from 300 down to 1.8 K using the relaxation technique. Measurements were extended to 0.06 K using a dilution refrigerator attachment.

**Theoretic simulations:** The electronic structure of Cs<sub>3</sub>V<sub>9</sub>Te<sub>13</sub> was calculated using density functional theory (DFT) as implemented in the Vienna ab initio Simulation Package (VASP)<sup>35</sup>. The experimentally determined crystal structure was fully relaxed until the residual forces on each atom were smaller than 5 meV/ $\text{\AA}$ . Van der Waals interactions were included using the zero-damping Grimme correction<sup>36</sup> during structural optimization. The ground-state magnetic order is identified as A-type antiferromagnetism, with the V spin moments aligned ferromagnetically within the *ab* plane and antiferromagnetically along the out-of-plane direction. This magnetic configuration is therefore used in the electronic structure calculations. The exchange–correlation potential was treated within the generalized gradient approximation PBE<sup>37</sup> in the structure relaxation and meta-generalized-gradient approximation SCAN<sup>38</sup> in band structure calculation. A plane-wave energy cutoff of 300 eV was employed, and the Brillouin zone was sampled using a 5 $\times$ 5 $\times$ 7 k-point mesh. The spin-orbit coupling is omitted throughout.

## Acknowledgments

We thank Yanpeng Qi, Chi-Ming Yim, Jing Tao, Rong Yu, Yu Wang, Yaobo Huang, and Baiqing Lv for helpful discussions. This work was supported by the National Key R&D of China under 2022YFA1402702 and 2021YFA1401600, National Natural Science Foundation of China with Grants Nos. 12334008, and 12374148. S. G. acknowledges the financial support from the National Natural Science Foundation of China (22205091), the Guangdong Pearl River Talent Plan (2023QN10C793). H. T. is supported by the National Natural Science Foundation of China (12574270) and Science and Technology Commission of Shanghai Municipality (No. 24PJA051).

## References

1. Guo, S. *et al.* Magnetic compounds with exotic Archimedean lattices. *Innovation* **6**, 100981 (2025).
2. Yu, U. Ising antiferromagnet on the archimedean lattices. *Phys. Rev. E* **91**, 62121 (2015).
3. Hor, P. H. *et al.* Superconductivity above 90 K in the square-planar compound system  $ABa_2Cu_3O_{6+x}$  with  $A = Y, La, Nd, Sm, Eu, Gd, Ho, Er$  and  $Lu$ . *Phys. Rev. Lett.* **58**, 1891–1894 (1987).
4. Sun, H. Signatures of superconductivity near 80 K in a nickelate under high pressure. *Nature* **621**, 493–498 (2023).
5. Chen, L. *et al.* Evidence for dirac fermions in a honeycomb lattice based on silicon. *Phys. Rev. Lett.* **109**, 56804 (2012).
6. Bauernfeind, M. *et al.* Design and realization of topological dirac fermions on a triangular lattice. *Nat. Commun.* **12**, 5396 (2021).
7. Balents, L. Spin liquids in frustrated magnets. *Nature* **464**, 199–208 (2010).
8. Yin, J.-X., Lian, B. & Hasan, M. Z. Topological kagome magnets and superconductors. *Nature* **612**, 647–657 (2022).
9. Hu, Y. *et al.* Non-trivial band topology and orbital-selective electronic nematicity in a titanium-based kagome superconductor. *Nat. Phys.* **19**, 1827–1833 (2023).
10. Li, Z. *et al.* Realization of flat band with possible nontrivial topology in electronic kagome lattice. *Science Advances* **4**, eaau4511 (2018).
11. Ortiz, B. R. *et al.* New kagome prototype materials: discovery of  $KV_3Sb_5$ ,  $RbV_3Sb_5$ , and  $CsV_3Sb_5$ . *Phys. Rev. Materials* **3**, 094407 (2019).
12. Mielke, C. *et al.* Time-reversal symmetry-breaking charge order in a kagome superconductor. *Nature (London)* **602**, 245–250 (2022).

13. Chen, H. *et al.* Roton pair density wave in a strong-coupling kagome superconductor. *Nature* **599**, 222–228 (2021).
14. Tan, H., Liu, Y., Wang, Z. & Yan, B. Charge Density Waves and Electronic Properties of Superconducting kagome Metals. *Physical Review Letters* **127**, 046401 (2021).
15. Liu, Y. *et al.* Superconductivity under pressure in a chromium-based kagome metal. *Nature* **632**, 1032–1037 (2024).
16. Liu, L. *et al.* A metastable pentagonal 2D material synthesized by symmetry-driven epitaxy. *Nat. Mater.* **23**, 1339–1346 (2024).
17. Heine, T. Pentagonal two-dimensional lattices. *Nat. Mater.* **23**, 1305–1306 (2024).
18. Ortiz, B. R. *et al.* CsV<sub>3</sub>Sb<sub>5</sub>: A Z<sup>2</sup> Topological kagome Metal with a Superconducting Ground State. *Physical Review Letters* **125**, 1 (2020).
19. Ortiz, B. R. *et al.* Superconductivity in the Z 2 kagome metal KV 3 Sb 5. *Phys. Rev. Mater.* **5**, 34801 (2021).
20. Silversmit, G., Depla, D., Poelman, H., Marin, G. B. & De Gryse, R. Determination of the V2p XPS binding energies for different vanadium oxidation states (V<sup>5+</sup> to V<sup>0+</sup>). *J. Electron Spectrosc. Relat. Phenom.* **135**, 167–175 (2004).
21. Georges, A., Medici, L. D. & Mravlje, J. Strong correlations from hund’s coupling. *Annu. Rev. Condens. Matter Phys.* **4**, 137–178 (2013).
22. Li, Y. *et al.* Electron correlation and incipient flat bands in the kagome superconductor CsCr<sub>3</sub>Sb<sub>5</sub>. *Nature Communications* **16**, 3229–8 (2025).
23. Shi, Y.-Q. *et al.* Superconductivity in metastable K<sub>1+δ</sub>Mo<sub>6</sub>Se<sub>8</sub> : a potassium-intercalated chevrel phase. *J. Am. Chem. Soc.* **147**, 22453–22459 (2025).
24. Yang, K. *et al.* Charge fluctuations above T CDW revealed by glasslike thermal transport in kagome metals AV<sub>3</sub>Sb<sub>5</sub> ( A = K , Rb , Cs ). *Phys. Rev. B* **107**, 184506 (2023).
25. Oh, D. *et al.* Hund’s flat band in a frustrated spinel oxide. *Proc. Natl. Acad. Sci.* **122**, e2518213122 (2025).
26. Kondo, S. *et al.* LiV<sub>2</sub>O<sub>4</sub> : a heavy fermion transition metal oxide. *Phys. Rev. Lett.* **78**, 3729–3732 (1997).
27. Hu, Y. *et al.* Rich nature of van hove singularities in kagome superconductor CsV<sub>3</sub>Sb<sub>5</sub>. *Nat. Commun.* **13**, 2220 (2022).
28. Kang, M. *et al.* Twofold van hove singularity and origin of charge order in topological kagome superconductor CsV<sub>3</sub>Sb<sub>5</sub>. *Nat. Phys.* **18**, 301–308 (2022).
29. Tan, H. & Yan, B. Abundant Lattice Instability in kagome Metal ScV<sub>6</sub>Sn<sub>6</sub>. *Phys. Rev. Lett.* **130**, 266402 (2023).

30. Ran, Y., Hermele, M., Lee, P. A. & Wen, X.-G. Projected-wave-function study of the spin-1/2 heisenberg model on the kagomé lattice. *Phys. Rev. Lett.* **98**, 117205 (2007).
31. Dissanayaka Mudiyanse, R. S. *et al.* LiYbSe<sub>2</sub>: Frustrated Magnetism in the Pyrochlore Lattice. *J. Am. Chem. Soc.* **144**, 11933–11937 (2022).
32. Zheng, L. *et al.* Emergent charge order in pressurized kagome superconductor CsV<sub>3</sub>Sb<sub>5</sub>. *Nature* **611**, 682–687 (2022).
33. Bourhis, L. J., Dolomanov, O. V., Gildea, R. J., Howard, J. A. K. & Puschmann, H. The anatomy of a comprehensive constrained, restrained refinement program for the modern computing environment – *Olex2* dissected. *Acta Crystallogr., Sect. A: Found. Adv.* **71**, 59–75 (2015).
34. Dolomanov, O. V., Bourhis, L. J., Gildea, R. J., Howard, J. a. K. & Puschmann, H. OLEX2: a complete structure solution, refinement and analysis program. *J. Appl. Crystallogr.* **42**, 339–341 (2009).
35. Kresse, G. & Furthmüller, J. Efficiency of ab-initio total energy calculations for metals and semiconductors using a plane-wave basis set. *Comput. Mater. Sci.* **6**, 15–50 (1996).
36. Grimme, S., Antony, J., Ehrlich, S. & Krieg, H. A consistent and accurate *ab initio* parametrization of density functional dispersion correction (DFT-D) for the 94 elements H-Pu. *J. Chem. Phys.* **132**, 154104 (2010).
37. Perdew, J. P., Burke, K. & Ernzerhof, M. Generalized gradient approximation made simple. *Phys. Rev. Lett.* **77**, 3865–3868 (1996).
38. Sun, J., Ruzsinszky, A. & Perdew, J. P. Strongly constrained and appropriately normed semilocal density functional. *Phys. Rev. Lett.* **115**, 36402 (2015).

# Supporting Information

**Table S1** Crystal Data and Structure Refinements for Cs<sub>3</sub>V<sub>9</sub>Te<sub>13</sub> (CVT) at 30, 100 and 300 K.

Empirical formula	Cs <sub>3</sub> V <sub>9</sub> Te <sub>13</sub>		
Formula weight	2516.09	2515.99	2516.09
Temperature/K	30	100	300
Crystal system	Hexagonal	Hexagonal	Hexagonal
Space group	<i>P</i> -62 <i>m</i> (189)	<i>P</i> -62 <i>m</i> (189)	<i>P</i> -62 <i>m</i> (189)
<i>a</i> /Å	10.1371(5)	10.1217(5)	10.089(3)
<i>c</i> /Å	8.1465(5)	8.1481(7)	8.212(3)
$\gamma$ [°]	120	120	120
volume/Å <sup>3</sup>	724.98(8)	722.93(9)	723.9(5)
Z	1	1	1
$\rho_{\text{calc}}$ / g/cm <sup>3</sup>	5.763	5.779	5.771
$\mu$ /mm <sup>-1</sup>	19.286	19.341	19.315
F(000)	1048	1048	1048
Mo K $\alpha$ radiation/Å	0.71073	0.71073	0.71073
2 $\theta$ range for data collection/°	4.64 to 52.99	4.65 to 53.94	4.66 to 54.95
Goodness-of-fit	1.188	1.142	1.104
Largest diff peak and hole (e/Å <sup>3</sup> )	2.42 and -1.52	1.88 and -0.61	1.77 and -1.17
Final R indexes [ $I \geq 2\sigma(I)$ ]	$R_1 = 0.0309$ , $wR_2 = 0.0869$	$R_1 = 0.0180$ , $wR_2 = 0.0420$	$R_1 = 0.0294$ , $wR_2 = 0.0685$
Final R indexes [all data]	$R_1 = 0.0314$ , $wR_2 = 0.0872$	$R_1 = 0.0189$ , $wR_2 = 0.0427$	$R_1 = 0.0304$ , $wR_2 = 0.0692$

**Table S2** Fractional atomic coordinates and equivalent isotropic displacement parameters (Å<sup>2</sup>) or CVT at 300 K..

Atom	x	y	z	U <sub>eq</sub>
Cs1	0.36401(19)	0.36401(19)	0	0.0336(4)
Te1	2/3	1/3	0.25265(16)	0.0194(3)
Te2	0	0.22819(10)	0.71992(13)	0.0168(3)
Te3	0.41185(15)	0.41185(15)	1/2	0.0343(5)
V1	0.1555(4)	0.1555(4)	1/2	0.0151(8)
V2	0.8210(3)	0.2866(3)	1/2	0.0172(6)

**Table S3** Crystal Data and Structure Refinements for Rb<sub>3</sub>V<sub>9</sub>Te<sub>13</sub> (RVT) at 300 K.

Empirical formula	Rb <sub>3</sub> V <sub>9</sub> Te <sub>13</sub>
Formula weight	2373.67
Temperature/K	298(2)
Crystal system	Orthorhombic
Space group	<i>Cmcm</i>
<i>a</i> /Å	17.5489(13)
<i>b</i> /Å	10.1022(8)
<i>c</i> /Å	15.8691(13)
volume/Å <sup>3</sup>	2813.3(4)
<i>Z</i>	4
$\rho_{calc}/\text{g/cm}^3$	5.604
$\mu/\text{mm}^{-1}$	21.211
<i>F</i> (000)	3976.0
Mo K $\alpha$ radiation/Å	0.71073
2 $\theta$ range for data collection/ $^\circ$	4.64 to 55.00
Goodness-of-fit on <i>F</i> <sup>2</sup>	1.025
Largest diff peak and hole (e/Å <sup>3</sup> )	2.148 and -1.519
Final <i>R</i> indexes [ <i>I</i> ≥ 2 $\sigma$ ( <i>I</i> )]	<i>R</i> <sub>1</sub> =0.0327, <i>wR</i> <sup>2</sup> =0.0650
Final <i>R</i> indexes [all data]	<i>R</i> <sub>1</sub> =0.0439, <i>wR</i> <sup>2</sup> =0.0701

**Table S4** Fractional atomic coordinates and equivalent isotropic displacement parameters (Å<sup>2</sup>) for RVT at 300 K.

Atom	x	y	z	U <sub>eq</sub>	Occupancy
Te1	0.66640(3)	0.33796(6)	0.62023(3)	0.02561(15)	1
Te2	0.38528(3)	0.72407(5)	0.63700(3)	0.01983(14)	1
Te3	0	0.56919(7)	0.86402(5)	0.01993(18)	1
Te4	0.79518(6)	0.54361(10)	0.77289(14)	0.0463(9)	0.5
Te5	1/2	0.42951(14)	0.77332(16)	0.0418(9)	0.5
Rb1	1/2	1/2	1/2	0.0516(6)	1
Rb2	0.82328(9)	1/2	1/2	0.0465(4)	1
V1	0.92399(11)	0.41591(17)	3/4	0.0186(4)	1
V2	0.76591(11)	0.28358(18)	3/4	0.0188(4)	1
V3	0.64462(11)	0.51489(18)	3/4	0.0184(4)	1
V4	1/2	0.6867(2)	3/4	0.0177(6)	1
V5	0.41074(11)	0.21761(18)	3/4	0.0184(4)	1

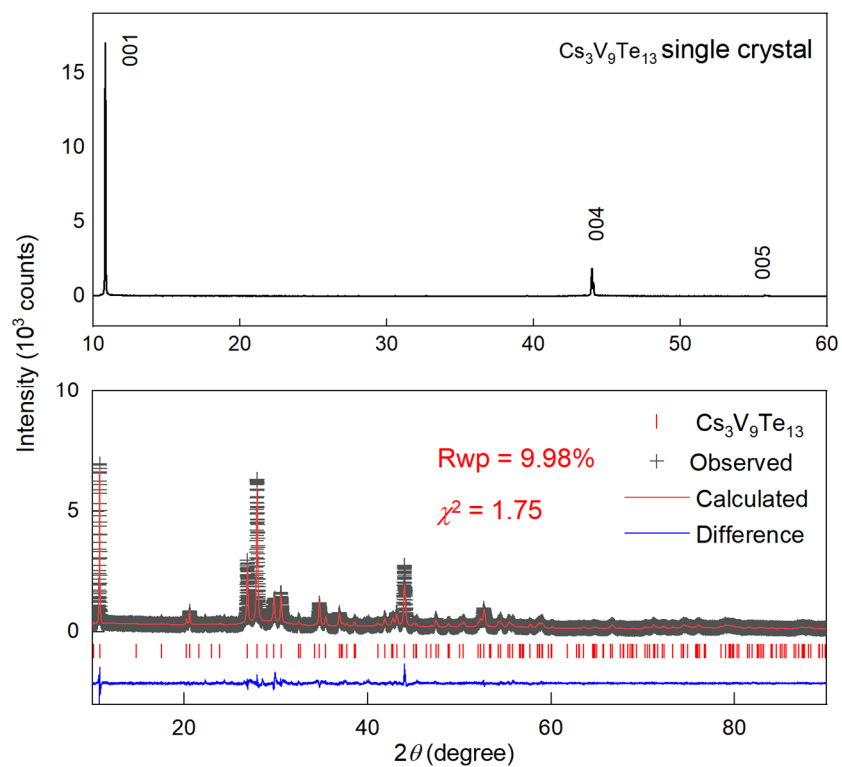


Figure S1 X-ray diffraction pattern of the CVT single crystal.

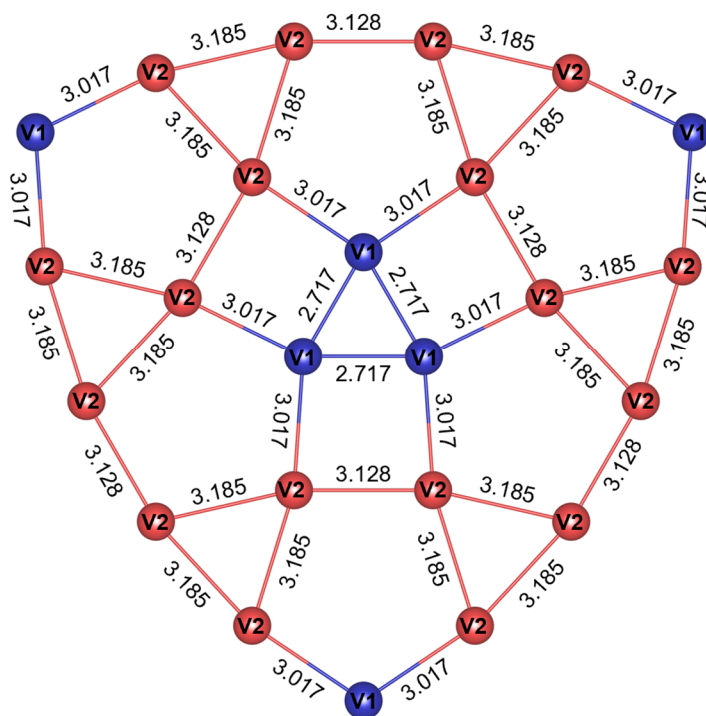
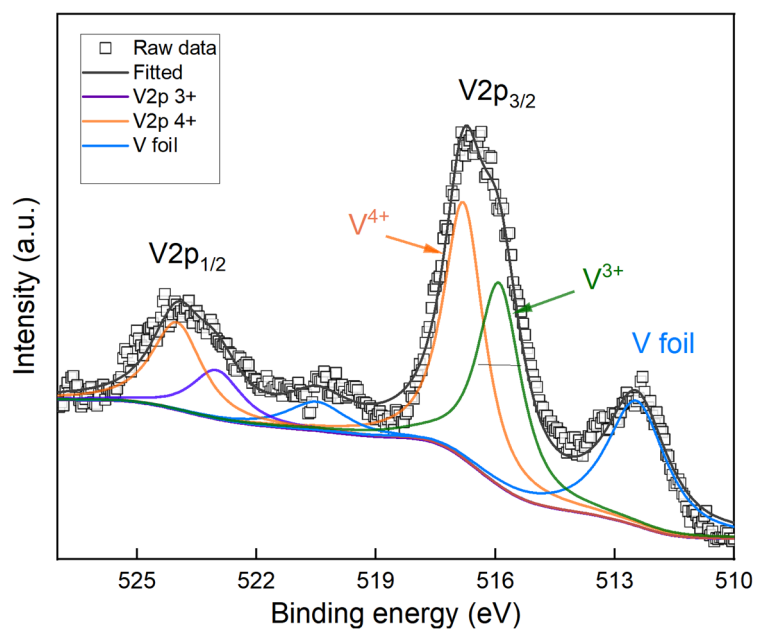
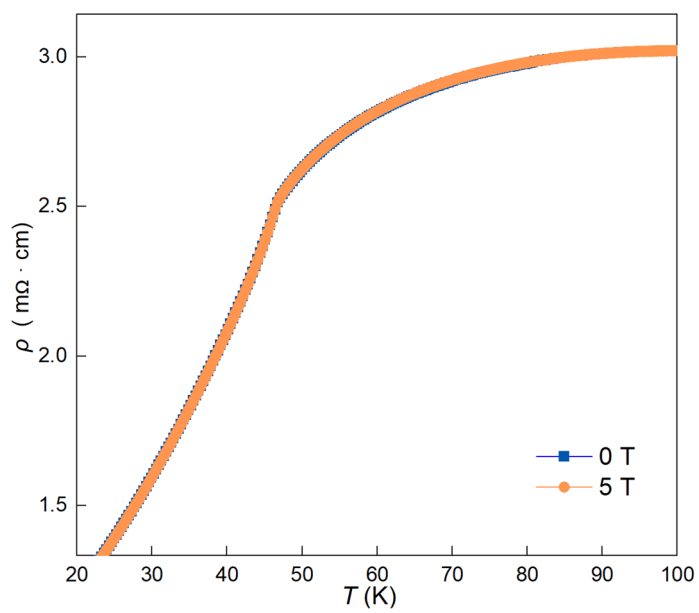


Figure S2 mosaic lattice details for CVT.



**Figure S3** XPS spectra for  $\text{Cs}_3\text{V}_9\text{Te}_{13}$  single crystal



**Figure S4** Temperature-dependent resistivity under different magnetic fields.

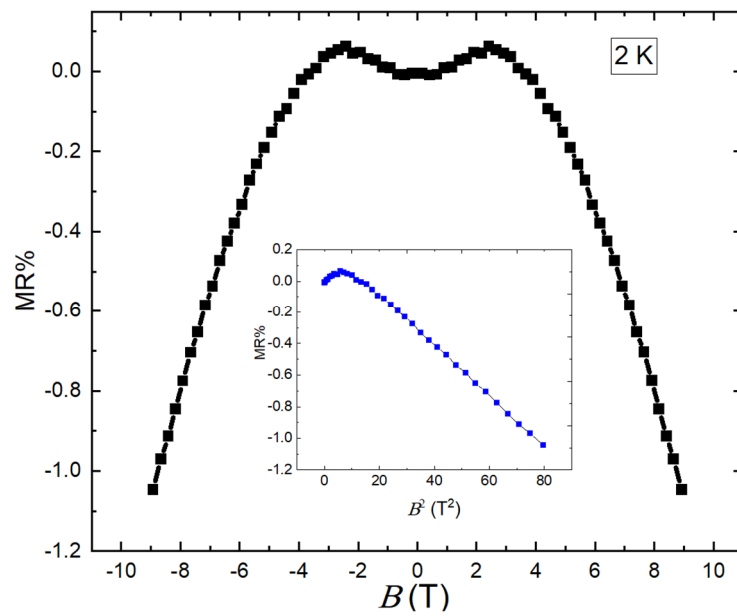


**Figure S5** Magnetoresistance (MR) versus magnetic field at 2 K.

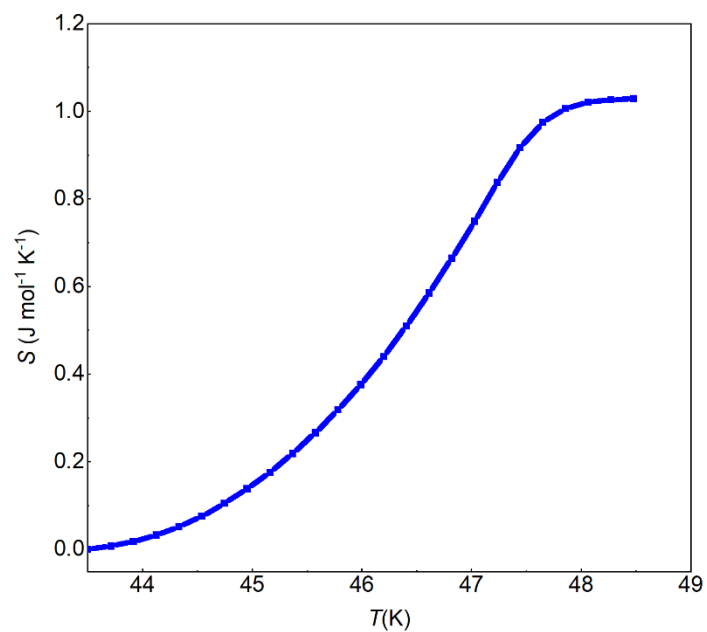


**Figure S6** Temperature dependence of the entropy change.

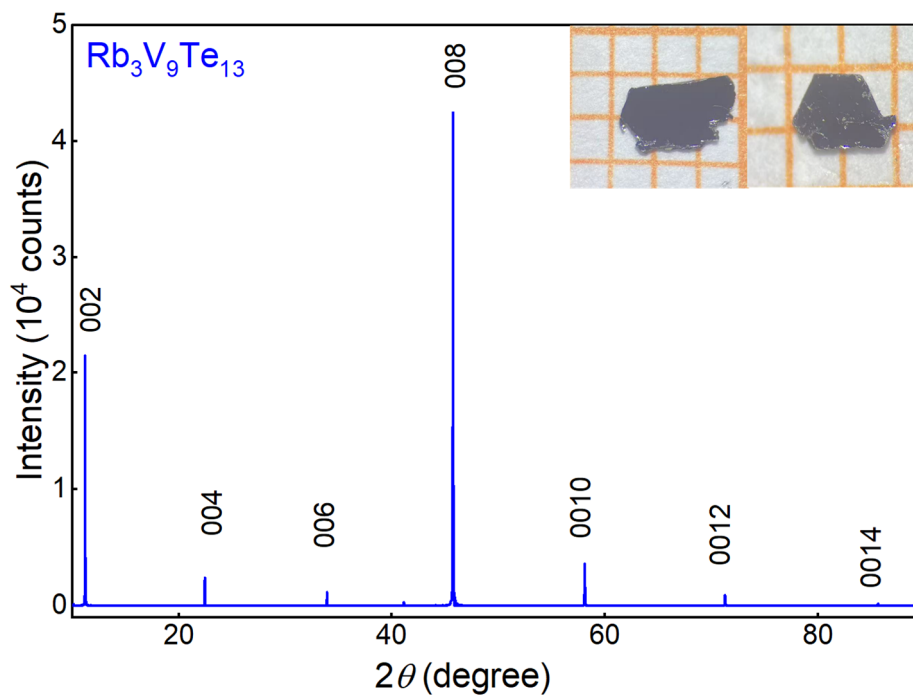


**Figure S7** X-ray diffraction pattern of the RVT single crystal.

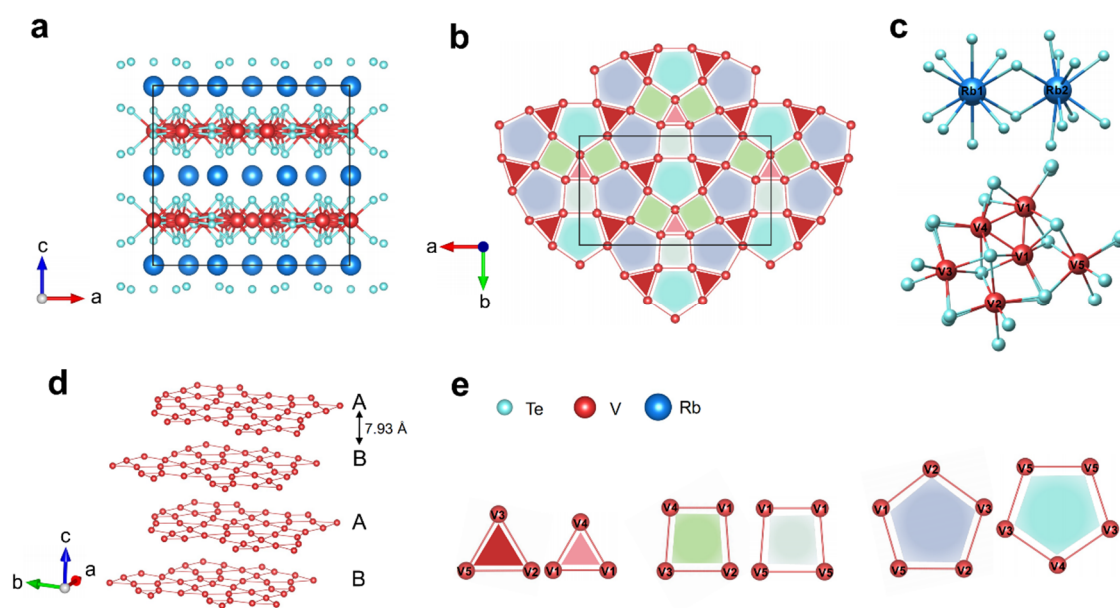


**Figure S8** Crystal structure of RVT. (a) 3D framework of RVT. (b) The V-based 2D mosaic Lattice. (c) Coordination environments for Rb and V atoms, respectively. (d) The stacking form of V-based layers. (e) Constituent triangular, square, and pentagonal units in a 2D mosaic Lattice.

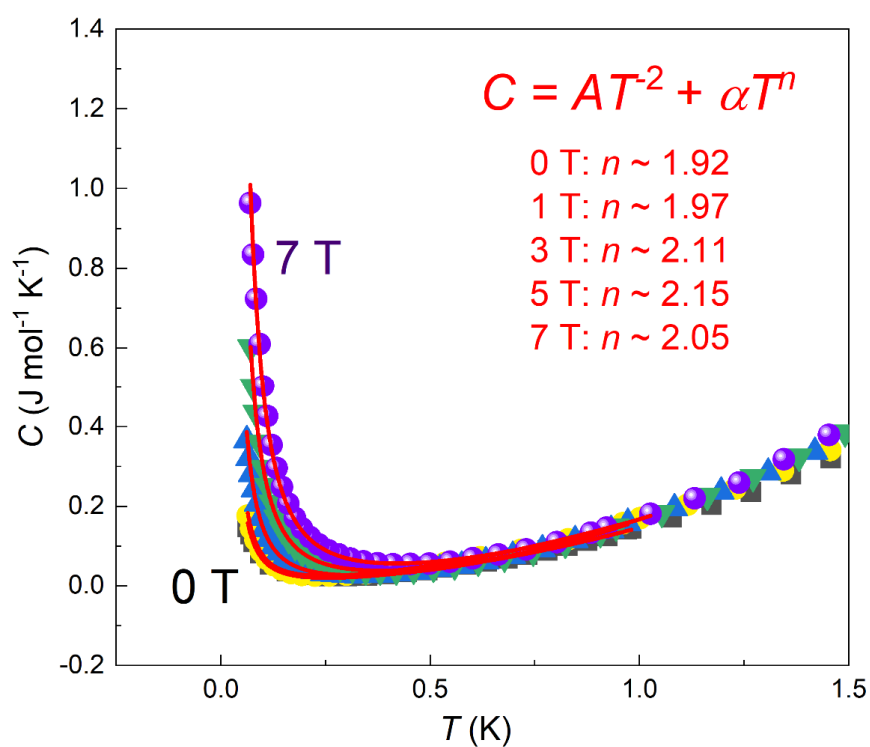


**Figure S9** Temperature dependence of the specific heat of RVT measured under different magnetic fields over a temperature range of 60 mK to 1.5 K. The red line represents a fit to the equation  $C = AT^{-2} + \alpha T^n$ .